

Supplementary Information

Cation- and lattice-site-selective magnetic depth profiles of ultrathin $\text{Fe}_3\text{O}_4(001)$ films

Tobias Pohlmann, Timo Kuschel, Jari Rodewald, Jannis Thien, Kevin Ruwisch, Florian Bertram, Eugen Weschke, Padraic Shafer, Joachim Wollschläger and Karsten Küpper

A. XMCD DATA FROM BESSY-II

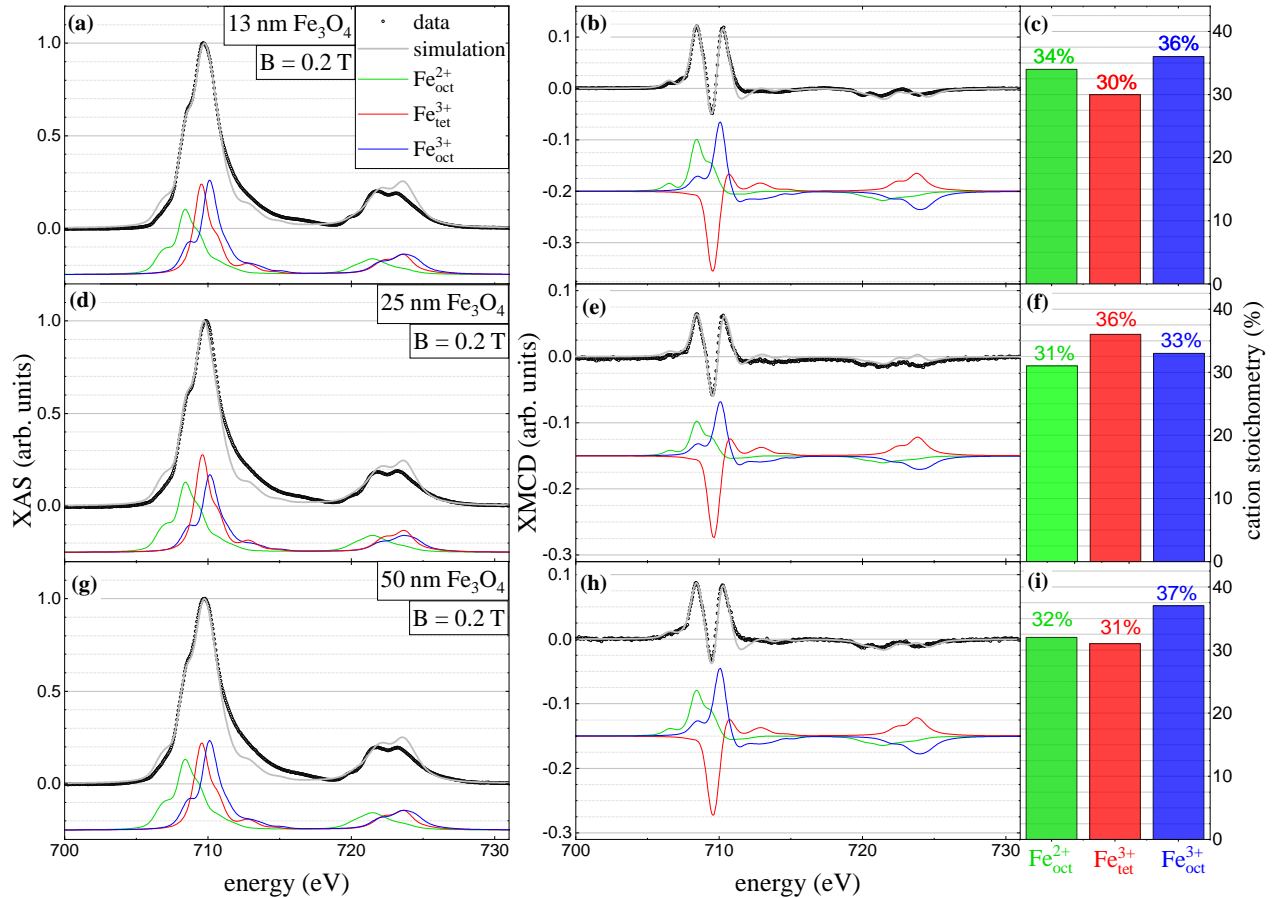


FIG. S1. XAS and XMCD spectra together with multiplet simulations and the extracted cation stoichiometry for (a)-(c) the 13 nm Fe_3O_4 film, (d)-(f) the 25 nm Fe_3O_4 film and (g)-(i) the 50 nm Fe_3O_4 film, recorded immediately before the XRMR measurements at BESSY, in a magnetic field of about $B \approx 200$ mT at the sample location. The multiplet calculations were done using the parameters in Tab. S1.

The XAS/XMCD data displayed in Fig. 1 of the main text were recorded at ALS in a 4 T vector magnet, making sure to saturate the sample magnetization for a reliable sum-rule evaluation. Also, since this endstation is dedicated to and optimized for XMCD, the data have better signal-to-noise ratio than those taken at UE46_PGM-1 of BESSY II, which specializes in resonant diffraction. For the XRMR measurements at UE46_PGM-1, the samples were located in between two permanent magnets with a magnetic field of about 200 mT at the sample location. We recorded there XAS/XMCD by the TEY detection scheme as well, in order to identify the energies of the XMCD extrema. These XAS and XMCD measurements, which were recorded alongside the XRMR, together with the multiplet fits and the resulting cation stoichiometry, are plotted in Fig. S1(a)-(c) for the 13 nm Fe_3O_4 film, in Fig. S1(d)-(f) for the 25 nm Fe_3O_4 film and in Fig. S1(g)-(i) for the 50 nm Fe_3O_4 film. We measured XAS spectra with both right and left

circularly polarized x-rays, $\text{XAS}^{\text{right}}$ and XAS^{left} . The non-dichroic XAS spectra shown in this work are the sum of these two XAS spectra, and the XMCD spectra their difference:

$$\text{XAS} = \text{XAS}^{\text{right}} + \text{XAS}^{\text{left}} \quad \text{XMCD} = \text{XAS}^{\text{right}} - \text{XAS}^{\text{left}}$$

Both are normalized so that the XAS maximum equals 1.

TEY data often suffer from saturation effects, when the absorption cross-section $\mu_A(E)$ directly at the $L_{2,3}$ edge becomes similar to the inverse electron escape depth $1/\lambda_e$. These difficulties in our data are corrected by the method described in Ref. [1]: the edge jump of the data is scaled to literature values [2] in order to obtain the saturation-affected $\mu'_A(E)$, and then

$$\mu_A(E) = \left(\frac{1}{\mu'_A(E)} - \lambda_e \right)^{-1} \quad (\text{S1})$$

is used to obtain the saturation-corrected absorption cross-section $\mu_A(E)$. We used $\lambda_e = 30 \text{ \AA}$, which was obtained from the damping of the Ni $L_{2,3}$ TEY signal in $\text{Fe}_3\text{O}_4/\text{NiO}/\text{MgO}$ bilayer samples. After that, a step function has been subtracted from the XAS spectra in order to compare it to the multiplet simulations.

Multiplet fits were done using the same parameter set for both the ALS and the BESSY II data. We assumed the three-cation model, with crystal field energies of 10Dq^{oct} in octahedral and 10Dq^{tet} in tetrahedral coordination, and the splittings between the initial and final charge-transfer states Δ_{init} and Δ_{final} . The exchange splitting $g \cdot \mu_B$ had to be set individually. They are the same ones as in Ref. [3], but can also be found in Tab. SI. In order to compare the calculations with the data, a Gaussian instrument broadening of 0.2 eV, and a Lorentzian lifetime broadening of 0.3 eV for L_3 and 0.6 eV for L_2 were assumed. The exchange field $g \cdot \mu_B$ of the simulations is smaller for the data taken at BESSY II compared to those from ALS. This indicates that our samples could not be fully saturated in a magnetic field of 200 mT used for the experiments at BESSY II.

Within the accuracy of the method, the cation stoichiometry is very much the same for all three samples. This means that the magnetically enhanced layer for the two Fe^{3+} species is not well observable by this evaluation. Instead we observe a cation stoichiometry very close to the ideal 1:1:1 ratio expected for Fe_3O_4 .

TABLE SI. Parameters used for the multiplet calculation. For comparison with the data, a Gaussian instrument broadening of 0.2 eV, and a Lorentzian lifetime broadening of 0.3 eV for L_3 and 0.6 eV for L_2 were assumed.

	10Dq^{oct}	10Dq^{tet}	Δ_{init}	Δ_{final}	$g \cdot \mu_B$ (BESSY II)	$g \cdot \mu_B$ (ALS)
13 nm	1.0 eV	-0.6 eV	6 eV	5 eV	0.028 eV	0.04 eV
25 nm	1.0 eV	-0.6 eV	6 eV	5 eV	0.011 eV	0.04 eV
50 nm	1.0 eV	-0.6 eV	6 eV	5 eV	0.016 eV	0.04 eV

B. XRR/XRMR STUDIES ON 13 NM AND 50 NM Fe_3O_4 FILMS

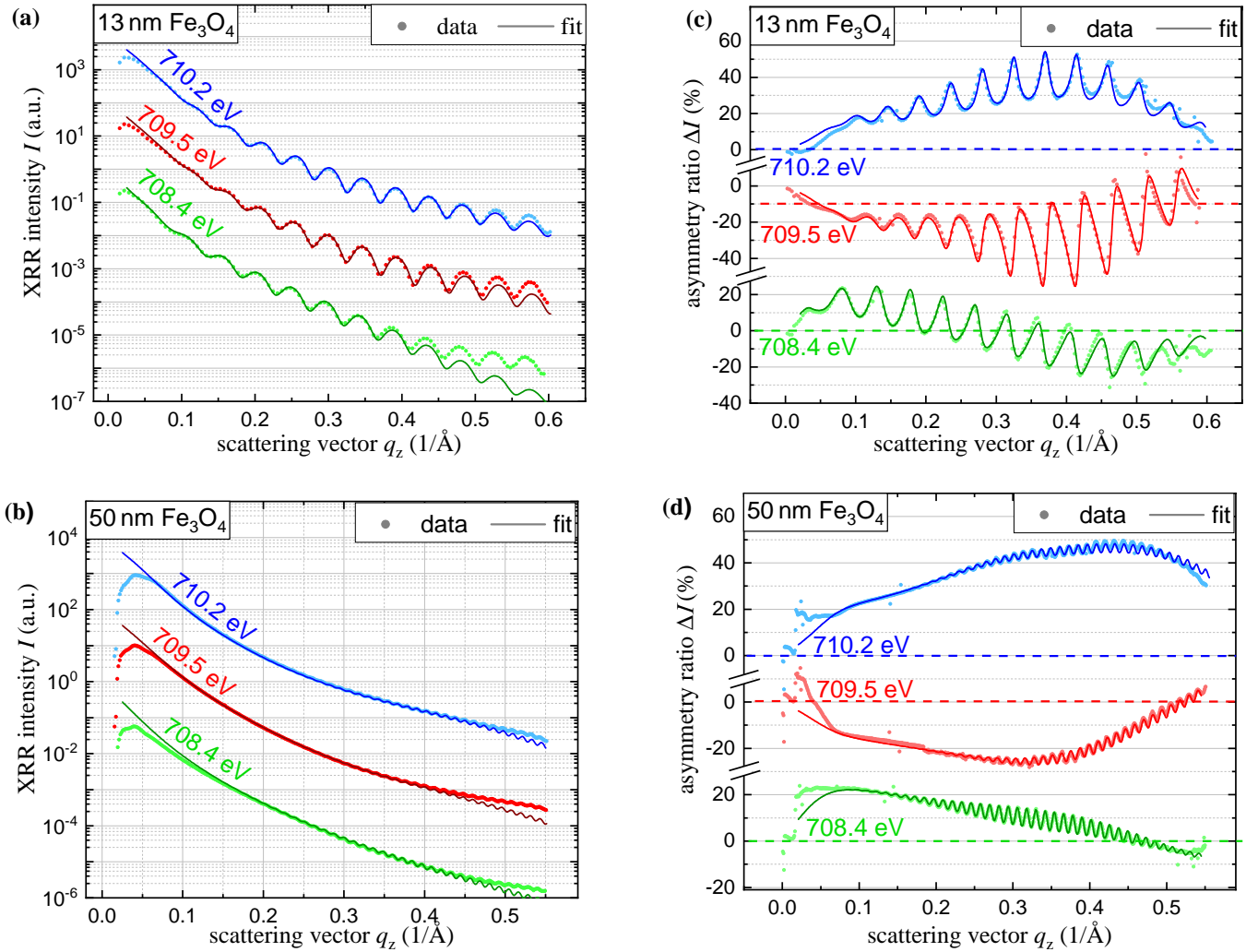


FIG. S2. XRR and XRMR data for the 13 nm and 50 nm Fe_3O_4 films. The non-dichroic XRR curves with their fits are shown for the 13 nm Fe_3O_4 film in (a) and for the 50 nm Fe_3O_4 film in (b), and the XRMR asymmetry ratios together with fits are displayed for the 13 nm in (c) and for the 50 nm Fe_3O_4 film in (d). The asymmetry fits are obtained by using the magneto-optical depth profiles in Fig. 3(a) in the main text.

Figure S2 displays XRR and XRMR data for the 13 nm and 50 nm Fe_3O_4 films, which were not included in the main text, where these data were only discussed exemplarily for the 25 nm Fe_3O_4 film. Figures S2(a) and (b) show the non-dichroic, resonant XRR data for the 13 nm and 50 nm Fe_3O_4 films, respectively. Figures S2(c) and (d) show the corresponding XRMR asymmetry ratios for those samples, together with the fits obtained from the magneto-optical depth profiles in Fig. 3(a) in the main text. Experimental data are fitted well except for small deviations for high scattering vectors, when the reflectivity becomes weak and the signal counts become comparable to the dark current of the photodiode detector. Overall, the model assuming top layers of enhanced magneto-optical absorptions works very well in fitting all XRMR data we recorded.

C. XRMR FITS WITH HOMOGENEOUS MAGNETIZATION

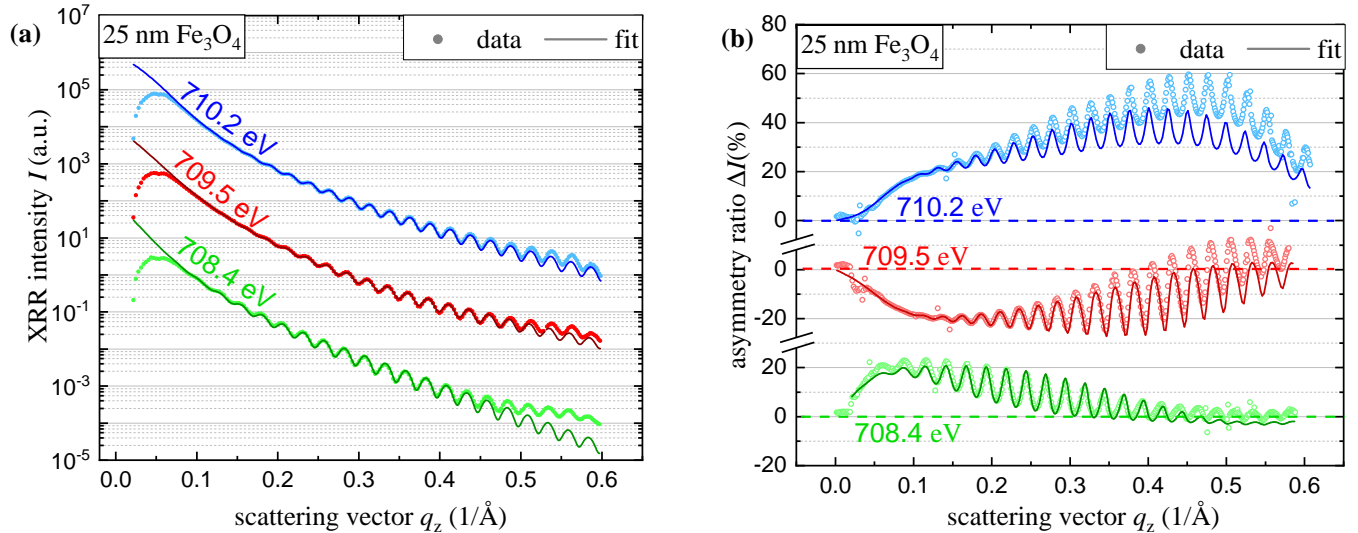


FIG. S3. (a) Non-dichroic XRR curves together with fits for the 25 nm Fe_3O_4 film, corresponding to the XRMR asymmetry ratios shown in Fig. 2 in the main text. (b) Asymmetry ratios of the 25 nm Fe_3O_4 film with the best fits achieved under the assumption of a single homogeneous magneto-optical profile. The curves at photon energies of 709.5 eV and 710.2 eV cannot be well accounted for already at scattering vectors $> 0.25 \text{ \AA}^{-1}$ without assuming a top layer of enhanced magneto-optical absorption (cf. Fig. 2 in the main text).

Figure S3(a) shows the resonant, non-dichroic XRR curves of the 25 nm Fe_3O_4 film together with their fits, which are the base for the asymmetry ratio fits in Fig. 2 in the main text. Non-dichroic XRR curves are obtained by averaging the XRR curves recorded with right and left circularly polarized x-rays, $I = (I^{\text{right}} + I^{\text{left}})/2$. The data are fitted well using a two-layer model, representing the Fe_3O_4 film and an optically thin 0.5 – 1 nm top layer, which is likely due to adsorbants on the surface, as obtained from non-resonant XRR, and again only become inaccurate for high scattering vectors. It has to be noted that at resonant energy and therefore high absorption, the XRR curves are dominated by the optical absorption of the film, while all other fit parameters have only small impact on the XRR curve. Consequently, these fits themselves do not provide a very exact insight in the structural details of the samples. For those, we recorded off-resonant XRR.

In order to strengthen our claim of a top layer of enhanced magnetization, Fig. S3(b) shows again the asymmetry ratios already seen in Fig. 2 of the main text, but this time together with fits assuming homogeneous magnetization depth profiles, without the top layer of enhanced magnetization. These fits are the best we could obtain by allowing variation of the magneto-optical constants $\Delta\beta$, $\Delta\delta$, individual roughnesses of the magneto-optical depth profiles at the substrate interface and the surface, as well as magnetic dead layers at both the substrate interface and the surface. While the fit for the 708.4 eV curve does hold up very well, demonstrating a homogeneous distribution of $\text{Fe}_{\text{Oct}}^{2+}$ cations, the other two fits - especially at 710.2 eV - cannot describe the data satisfyingly. In order to account for these behaviours, we need to assume the layer of magneto-optical enhancement at the surface (see Fig. 2 in the main text). The fact that the XRMR curves of all three measured samples can be fitted well with this assumption makes this a very convincing model.

D. SURFACE CATION VACANCY STRUCTURE

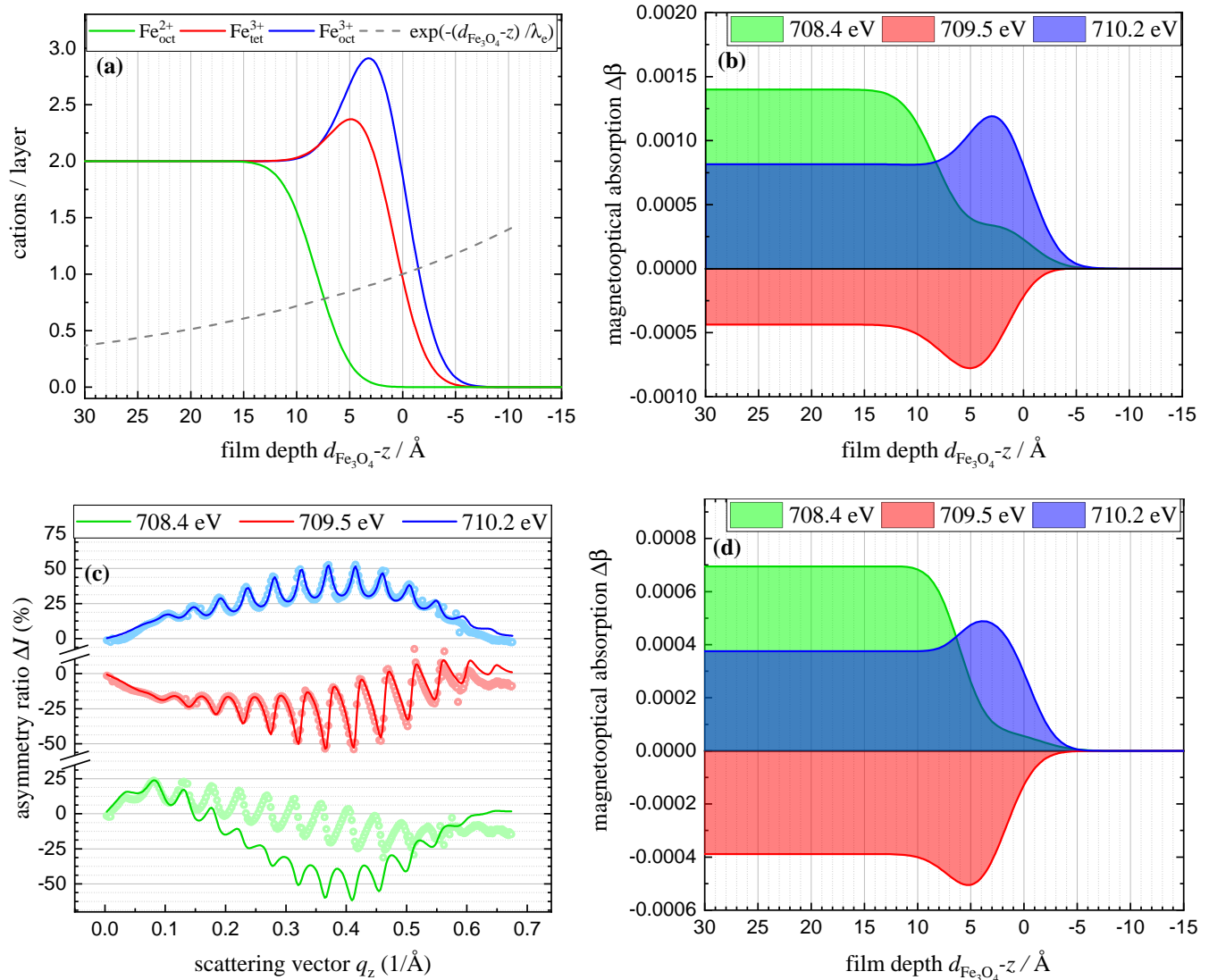


FIG. S4. (a) Cation depth profiles expected for a $\text{Fe}_3\text{O}_4(001)$ film with a SCV surface and a roughness of $\sigma^{\text{surf}} = 2.5 \text{ \AA}$. The dashed grey line shows the sensitivity of the TEY signal to electrons from film depth $d_{\text{Fe}_3\text{O}_4} - z$, $\exp(-(d_{\text{Fe}_3\text{O}_4} - z)/\lambda_e)$. (b) Expected magneto-optical depth profiles of the model film in (a) at the XMCD resonances 708.4 eV, 709.5 eV and 710.2 eV. (c) XRMR data from the 13 nm Fe_3O_4 film, together with fits produced by the magneto-optical depth profiles in (d). (d) Magneto-optical depth profiles which are meant to recreate the profiles in (b), but slightly adapted to provide fits to the data in (c). For the resonances at 709.5 eV and 710.2 eV, satisfactory results can be achieved by this model, but not for the resonance at 708.4 eV.

The magneto-optical depth profiles we find share some key features with the SCV structure of the $\text{Fe}_3\text{O}_4(001)$ surface [4], but are not fully identical with it. We want to emphasize that our samples had been exposed to air when the XRMR measurements were done, so a fully intact SCV surface is likely not present. In this chapter we present a thorough comparison of the SCV model to our findings. Along the [001] direction, the bulk structure of Fe_3O_4 consists of alternating layers containing $(2 \text{ Fe}_{\text{oct}}^{2+} + 2 \text{ Fe}_{\text{oct}}^{3+})$ per unit cell (u.c.) and $2 \text{ Fe}_{\text{tet}}^{3+}/\text{u.c.}$. DFT calculations of the SCV surface predict a different cation distribution in the first 4 cation layers: The first cation layer consists of $4 \text{ Fe}_{\text{oct}}^{3+}/\text{u.c.}$, the second layer of $3 \text{ Fe}_{\text{tet}}^{3+}/\text{u.c.}$, the third layer of $2 \text{ Fe}_{\text{oct}}^{3+}/\text{u.c.}$, and the fourth layer of $2 \text{ Fe}_{\text{tet}}^{3+}/\text{u.c.}$. From there, Fe_3O_4 continues with the cation distribution well-known from the bulk structure.

Figure S4(a) shows the cation profiles as expected from an ideal SCV-surface with a surface roughness $\sigma^{\text{surf}} = 2.5 \text{ \AA}$, corresponding to our films. Using the contributions of the cations to the XMCD spectrum in Tab. II of the main text,

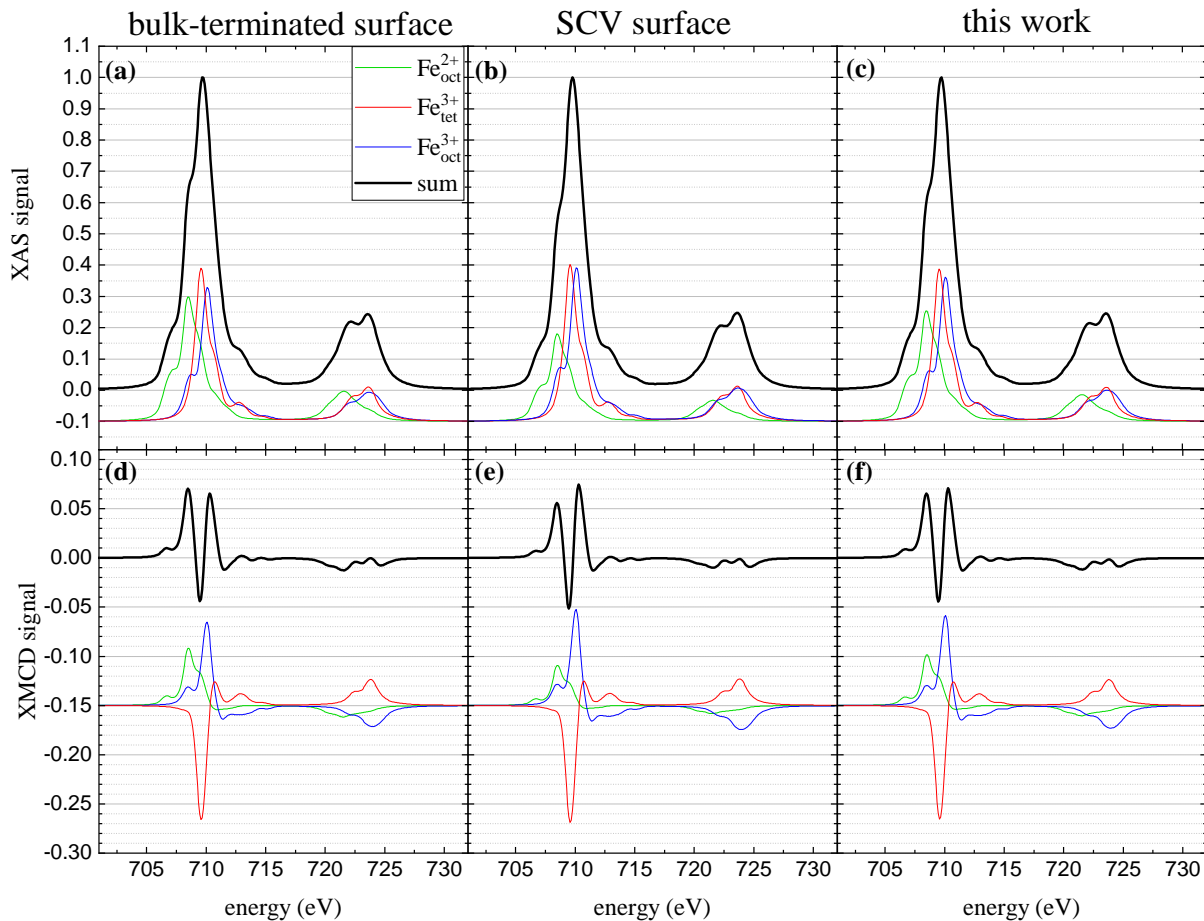


FIG. S5. Multiplet calculations of the XAS and XMCD spectra from (a),(d) a surface with bulk cation distribution, (b),(e) a SCV surface and (c),(f) the surface model we extract from the XRMR measurements in this work. They were calculated by weighting the individual cation spectra using Eq. S2 with corresponding cation depth profiles $c_{\text{cation}}(\zeta)$.

the expected magneto-optical depth profiles at the three XMCD resonances can be constructed, and are displayed in Fig. S4(b). We recreated models of these theoretical magneto-optical depth profiles, and fitted their resulting asymmetry ratios ΔI to the XRMR data of the 13 nm Fe_3O_4 film by retaining the main features of the SCV model. The XRMR data and fits are plotted in Fig. S4(c), and the magneto-optical depth profiles which produce them in Fig. S4(d). The fits for the resonances at 709.5 eV and 710.2 eV describe the data very well, but not at 708.4 eV. We can conclude that our data are consistent with the Fe^{3+} enrichment predicted by the SCV model, but not with the lack of Fe^{2+} .

An Fe^{3+} enrichment of the $\text{Fe}_3\text{O}_4(001)$ surface has some consequences for surface-sensitive techniques which are often utilized for the study of magnetite. We want to discuss this effect for the XAS and XMCD measurements used in this work. Figure S5 shows multiplet simulations of the XAS and XMCD spectra of Fe_3O_4 for three different surface compositions, assuming a TEY detection scheme. In TEY mode, the probing depth is limited by the electron escape depth λ_e , which is about 30 Å for Fe_3O_4 . In Fig. S4(a) the cation depth profiles $c_{\text{Fe}^{2+}_{\text{oct}}}(\zeta)$, $c_{\text{Fe}^{3+}_{\text{tet}}}(\zeta)$, $c_{\text{Fe}^{3+}_{\text{oct}}}(\zeta)$ for films with SCV surface are shown together with the exponential decay $\exp(-\zeta/\lambda_e)$ describing the contribution to the TEY signal from film depth $\zeta = d_{\text{Fe}_3\text{O}_4} - z$. Integration over their product yields a weight factor

$$\text{wgt}_{\text{cation}} = \int c_{\text{cation}}(\zeta) \cdot \exp(-\zeta/\lambda_e) d\zeta, \quad (\text{S2})$$

which we used to weight the individual spectra of the cations in Fig. S5.

Figure S5(a) and S5(d) show the XAS and XMCD spectra for a bulk-terminated surface with a 1:1:1 ratio of the three cations, S5(b) and S5(e) for an SCV surface as illustrated in S4(a), and S5(c) and S5(f) for the model extracted from the XRMR data in this work. For the multiplet simulations, we used the same parameters as for the fits to the

XMCD spectra of the 25 nm Fe_3O_4 film recorded at BESSY. They can be found in Tab. SI.

The XAS spectra differ only very slightly because of the strong overlap of the three individual spectra, and only the low-energy shoulder at the $\text{Fe}_{\text{oct}}^{2+}$ becomes less pronounced for the Fe^{3+} -rich surfaces. In the XMCD spectra, the change is more easily visible in the intensity difference of the resonances at 708.4 eV and 710.2 eV. This difference can lead to a slight underestimation of $\text{Fe}_{\text{oct}}^{2+}$ in a multiplet analysis. In fact, our XMCD spectra compare best with the model in Fig. S5(f), but the difference observed between Fig. S5(f) and Fig. S5(d) is well in the range of common sample-to-sample variation.

For the sum rule analysis, the impact can be expected to be small, since the underestimation of $\text{Fe}_{\text{oct}}^{2+}$ is compensated by an overestimation of $\text{Fe}_{\text{oct}}^{3+}$ of almost same extent in the XMCD signal.

-
- [1] T. J. Regan, H. Ohldag, C. Stamm, F. Nolting, J. Lüning, J. Stöhr, and R. L. White, *Phys. Rev. B* **64**, 214422 (2001).
 - [2] C. T. Chantler, *J. Phys. Chem Ref. Data* **24**, 71 (1995).
 - [3] K. Kuepper, O. Kuschel, N. Pathé, T. Schemme, J. Schmalhorst, A. Thomas, E. Arenholz, M. Gorgoi, R. Ovsyannikov, S. Bartkowski, G. Reiss, and J. Wollschläger, *Phys. Rev. B* **94**, 024401 (2016).
 - [4] R. Bliem, E. McDermott, and G. S. Parkinson, *Science* **346** (2014).